Eur. Phys. J. C 8, 135–150 (1999)
DOI 10.1007/s100529801039

THE EUROPEAN PHYSICAL JOURNAL C
© Springer-Verlag 1999

Wave functions and spectrum in hot electroweak matter for large Higgs masses

E.-M. Ilgenfritz,[1,a] A. Schiller,[2,b] C. Strecha[2,c]

[1] Institute for Theoretical Physics, Kanazawa University, Kanazawa 920-1192, Japan
[2] Institut für Theoretische Physik, Universität Leipzig, D-04109 Leipzig, Germany

Received: 4 August 1998 / Published online: 2 November 1998

Abstract. We present results for the wave functions and the screening mass spectrum for quantum numbers 0^{++}, 1^{--} and 2^{++} in the three-dimensional $SU(2)$–Higgs model near to the phase transition line below the endpoint and in the crossover region. Varying the $3D$ gauge couplings we study the behaviour along a line of constant physics towards the continuum limit in both phases. In the crossover region the changing spectrum of screening states versus temperature is examined showing the aftermath of the phase transition at lower Higgs mass. Different to smearing concepts we used large sets of operators with various extensions allowing to identify wave functions in position space.

1 Introduction

During the last years, due to efforts of three groups [1]-[5] using the $3D$ approach, various aspects of the high temperature electroweak phase transition have been explored in the $SU(2)$–Higgs model, with increasing Higgs mass M_H. The interface tension has been seen falling over three orders of magnitude [1,6] (if expressed as α/T_c^3), whereas the latent heat goes to zero roughly linearly with M_H. The continuum characteristics of the transition is difficult to obtain with the same precision by $4D$ Monte Carlo simulations [7], although the results are consistent with each other where they can be compared [8,6]. Approaching the W mass M_W, the character of the transition is now known to change drastically. It is the spectrum of physical excitations in this parameter region that we are going to study here.

The $4D$ lattice approach meets two problems which made the $3D$ approach so attractive. At first, only the bosonic sector can be studied because of the problems to deal with chiral fermions. Second, simulations are difficult due to the presence of different length scales. The inverse Matsubara frequency, $1/(2\pi T)$, is much shorter than the two correlation lengths, $1/m_W(T)$ and $1/m_H(T)$, with the screening masses differing strongly from the zero temperature masses M_W and M_H. If the temporal lattice extent N_τ should be not too small, they can be accommodated on a $4D$ lattice only if this is anisotropic. This requires more couplings to be tuned than in the isotropic case when one first has to match the M_H/M_W ratio and the renormalised coupling $g_4^2(\mu_4)$ on a $T=0$ ($N_\tau = N_s$) lattice.

[a] ilgenfri@hep.s.kanazawa-u.ac.jp
[b] schiller@tph204.physik.uni-leipzig.de
[c] strecha@tph204.physik.uni-leipzig.de

The $3D$ approach represents itself as a radical solution to both problems. It is based on perturbative dimensional reduction in the continuum combined with lattice perturbation theory [9], leaving to lattice simulation only the non-perturbative description of the softest modes whose behaviour governs the transition. All non-zero Matsubara modes are integrated out leaving an effective, superrenormalisable theory in $3D$ with the smallest length scale $1/(2\pi T)$ removed. Chiral fermions can be implicitly dealt with at this step. In a second step the next heaviest modes related to the Debye mass $m_D \sim g\,T$ (the A_0 components of the gauge field) are integrated out. Thus an effective $3D$ $SU(2)$–Higgs theory emerges with the action

$$S_3 = \int d^3x \Big(\frac{1}{4} F^b_{\mu\nu} F^b_{\mu\nu} + (D_\mu \phi)^+ (D_\mu \phi) + m_3^2 \phi^+ \phi + \lambda_3 (\phi^+ \phi)^2 \Big) . \quad (1)$$

It has dimensionful, renormalisation group invariant couplings g_3^2 and λ_3 and a running mass squared $m_3^3(\mu_3)$. It is put into correspondence to a lattice model with the action

$$S = \beta_G \sum_p \big(1 - \frac{1}{2}\mathrm{tr} U_p\big) - \beta_H \sum_{x,\mu} \frac{1}{2}\mathrm{tr}(\Phi_x^+ U_{x,\mu} \Phi_{x+\hat{\mu}}) + \sum_x \big(\rho_x^2 + \beta_R(\rho_x^2 - 1)^2\big) . \quad (2)$$

The lattice couplings are (with a suitable parameter M_H^*)

$$\beta_G = \frac{4}{a g_3^2} \, , \; \beta_R = \frac{\lambda_3}{g_3^2} \frac{\beta_H^2}{\beta_G} = \frac{1}{8} \left(\frac{M_H^*}{80\ \mathrm{GeV}} \right)^2 \frac{\beta_H^2}{\beta_G} \, ,$$
$$\beta_H = \frac{2(1-2\beta_R)}{6 + a^2 m_3^2} \, , \quad (3)$$

which can be expressed in terms of $4D$ couplings and masses. The parameter M_H^* is approximately equal to the zero temperature physical Higgs mass. The summation in (2) is taken over plaquettes p, sites x and links $l = \{x, \mu\}$. The gauge fields are represented by unitary 2×2 link matrices $U_{x,\mu}$ and U_p denotes the $SU(2)$ plaquette matrix. The Higgs field is parametrised as follows: $\Phi_x = \rho_x V_x$, where $\rho_x^2 = \frac{1}{2}\mathrm{tr}(\Phi_x^+ \Phi_x)$ is the Higgs modulus squared, and V_x is an element of the group $SU(2)$.

The bare mass squared is related to the renormalised $m_3^2(\mu_3)$ (we choose $\mu_3 = g_3^2$) through a lattice two-loop calculation [10] giving $m_3^2(\mu_3) = m_3^2 + m_{1-\mathrm{loop}}^2 + m_{2-\mathrm{loop}}^2$. The lattice results obtained in the $3D$ approach indicate the validity of the dimensional reduction (without additional operators in the action) near to the transition temperature for Higgs masses in the range between 30 and 240 GeV. The relations between the parameters of the effective $3D$ model and the physical quantities Higgs mass and temperature are derived in [9].

According to recent lattice studies [4,5,11] the standard electroweak theory ceases to possess a first order transition for a Higgs mass $M_H > 72$ GeV. Therefore, taking the newest lower bound of the Higgs mass into account [12], the standard model does not pass through a true phase transition at the electroweak vector boson mass scale. This and the small amount of CP violation in the standard model seem to rule out the possibility to explain the BAU generation without new physics. Therefore the phenomenological interest has moved to extensions of the standard model, with minimal supersymmetric extensions (MSSM) being the most promising variant. First interesting lattice results have been published recently [13].

From the point of view of non-perturbative physics in general, the lattice version of the standard Higgs model is still interesting as a laboratory for investigating the behaviour of hot gauge fields coupled to scalar matter, for the characterisation of possible bound states, for the understanding of real time topological transitions and the role of embedded topological defects [14] at the transition. It has been important as a cross-check for analytical approximation schemes and will be so in future.

We are concentrating in this paper on the qualitative change of the spectrum of screening states that happens across the phase transition and what remains of it in the crossover region (at somewhat higher Higgs mass). This would not be possible without a systematic evaluation of the wave functions in configuration space that, for the first time in this context, is attempted here. Some intermediate results have been published before [15].

The rest of this paper is organised as follows. In Sect. 2 we discuss the cross correlation technique and the operator set as we have used them. The wave functions and masses of the ground state and excited states near to the endpoint of the phase transition are presented in Sects. 3 and 4 for the symmetric and the Higgs phase at $M_H^* = 70$ GeV, respectively. This complements a recent study in [16] which has been performed, however, at much lighter ($M_H^* = 35$ GeV) Higgs mass. Section 5 contains our results for the dynamics of the spectrum with increasing temperature in the crossover region for $M_H^* = 100$ GeV, slightly above the endpoint of the first order transition, which can be compared with results of [17] obtained at a markedly larger Higgs mass $M_H^* \approx 120$ GeV. In Sect. 6 we summarise our results. The Appendices contain tables of the measured mass values obtained from this analysis and details how to construct the operator set for the quantum numbers in $2+1$ dimensions on the lattice.

2 The cross correlation technique in the $3D$ Model

To study simultaneously the ground state *and* excited states (as well as their wave functions) one has to consider cross correlations between (time-slice sums of) operators $\mathcal{O}_i$ from a complete set in a given J^{PC} channel with quantum numbers J (angular momentum) , P (parity) and C (charge conjugation). According to the transfer matrix formalism, one should be able to write the connected correlation matrix at time[1] separation t in the spectral decomposition form

$$C_{ij}(t) = \sum_{n=1}^{\infty} \Psi_i^{(n)} \Psi_j^{(n)*} e^{-m_n t} \tag{4}$$

with

$$\Psi_i^{(n)} = \langle \mathrm{vac} | \mathcal{O}_i | \mathbf{\Psi}^{(n)} \rangle \tag{5}$$

where $|\mathbf{\Psi}^{(n)}\rangle$ is the n-th (zero momentum) energy eigenstate. The vacuum state is dropped from this sum due to the connectedness of the correlator. By suitable diagonalisation this allows to find masses *and* wave functions of the lowest mass screening states (ground state) and higher mass excited states in the various J^{PC} channels.

However, in practice one has to choose a truncated set of operators $\mathcal{O}_i$, $(i = 1, \ldots, N)$. The hope is that the lowest lying states ($k = 1, \ldots, r$, with $r << N$) might not be essentially affected by the truncation and that their masses and wave functions can be approximately extracted from the direct eigenvalue problem for $C_{ij}(t)$

$$\sum_j C_{ij}(t) \Psi_j^{(n)} = \lambda^{(n)}(t) \Psi_i^{(n)}. \tag{6}$$

Experience shows that this solution suffers from big systematic truncation errors. Solving instead the generalised eigenvalue problem

$$\sum_j C_{ij}(t)\ \Psi_j^{(n)} = \lambda^{(n)}(t, t_0) \sum_j C_{ij}(t_0)\ \Psi_j^{(n)} \tag{7}$$

or

$$\sum_j \tilde{C}_{ij}(t, t_0) \tilde{\Psi}_j^{(n)} = \lambda^{(n)}(t, t_0) \tilde{\Psi}_i^{(n)}\,, \tag{8}$$

with

$$\tilde{C}_{ij}(t, t_0) = \left(C^{-\frac{1}{2}}(t_0) C(t) C^{-\frac{1}{2}}(t_0) \right)_{ij}\,, \tag{9}$$

[1] in the $3D$ approach "time" is x_3

($t > t_0$, where practically $t_0 = 0, 1, 2, ..$) errors related to this truncation can be kept minimal [18,19]. Practically the decomposition of the matrix $C(t_0)$ is performed using a Cholesky decomposition $C(t_0) = LL^T$. The remaining problem is that of diagonalizing a symmetric matrix $\tilde{C}(t, t_0) = L^{-1}C(t)L^{T\ -1}$ with rotated eigenvectors $\tilde{\Psi}^{(n)} = L^T\Psi^{(n)}$.

The optimised eigenfunctions $\Psi^{(n)}$ in the chosen operator basis (obtained with a small distance t_0) give an information about the overlap of the source operators $\mathcal{O}_i$ with the actual eigenstates $|\mathbf{\Psi}^{(n)}\rangle$. Due to truncation the eigenvectors of (7) are not supposed to be orthogonal to each other since $C^{-1}(t_0)C(t)$ is not a symmetric matrix. The components of the eigenvectors $\Psi_k^{(n)}$ ($n \leq N$) are effected by terms of the order $O(\exp(-m_{N+1}t))$, where N is the number of used operators. Only in the limit of a complete set of operators the eigenvectors become orthogonal. Therefore, the (non)orthogonality between different states provides a criterion for the completeness of the operator set.

The masses $m^{(n)}$ of these states are obtained by fitting not the eigenvalues $\lambda^{(n)}$ of (8) but the diagonal elements $\mu^{(n)}$,

$$\mu^{(n)}(t, t_0) = \sum_{ij} \tilde{\Psi}_i^{(n)}\ \tilde{C}_{ij}(t, t_0)\ \tilde{\Psi}_j^{(n)}\,, \qquad (10)$$

to a hyperbolic cosine form with t in some plateau region of a local effective mass that is defined as

$$m_{\rm eff}^{(n)}(t, t_0) = \log\frac{\mu^{(n)}(t, t_0)}{\mu^{(n)}(t+1, t_0)}\,. \qquad (11)$$

The wave function components with respect to the operator basis characterise the coupling of source operators $\mathcal{O}_i$ to the bound states (lowest mass or excited) in the J^{PC} channel. Using operators of different extension transverse to the correlation direction a spatial resolution of the optimised wave function can be achieved. Practically only a subset of operators with fixed quantum numbers can be included. The admitted operator set includes gauge invariant operators properly chosen with respect to the lattice symmetry and quantum numbers. For completeness, the choice of the gauge invariant operators in $2+1$ dimensions on the cubic lattice corresponding to the quantum numbers mentioned is discussed in Appendix A. Though the results might be in principle known a reasonable presentation for the lattice $SU(2)$–Higgs model similar to that of [23] for 3+1 dimensions was not available.

In order to associate a spatial structure to the states under study one has to use operators which correspond to various extension. One way is to define a set of operators using smearing techniques in several variants. In the present context this has been practised in [20,16,17], smearing gauge links and Higgs fields. The smearing parameter determines a well-defined mixture of various lengths in the source operator and has to be optimised by a variational procedure (strictly speaking, for all states separately).

In contrast to this smearing technique, we have chosen the other extreme and collected only a few types of operators $\mathcal{O}_i$ in our base (properly chosen with respect to lattice symmetry and quantum numbers) but with a wide span of sizes l in lattice spacings. Such a basis allows to obtain information on the spatial extension of a bound state without going through a variational procedure (for the lowest and the excited states). In principle, smearing the link and Higgs variables underlying these operators would be conceivable for further optimising the states under study. Here, we have restricted ourselves to Higgs strings and Wilson loops with varying spatial extent.

In the three quantum number channels investigated here we have admitted the following operators (with $\mu = 3$ reserved for the correlation direction, see Appendix A):

$$\begin{aligned}
0^{++}:\ & \rho_x^2\,, \\
& S_{x,1}(l) + S_{x,2}(l)\,, \\
& W_{x,1,2}(l) + W_{x,2,1}(l) \qquad (12)\\
& (\text{quadratic Wilson loops of size } l \times l)\,, \\
1^{--}:\ & V^b_{x,1}(l) + V^b_{x,2}(l)\,, \\
2^{++}:\ & S_{x,1}(l) - S_{x,2}(l)\,.
\end{aligned}$$

Here the following notation is used (l denotes the string length in lattice units)

$$S_{x,\mu}(l) = \frac{1}{2}\mathrm{tr}(\Phi_x^+ U_{x,\mu} \ldots U_{x+(l-1)\hat{\mu},\mu}\Phi_{x+l\hat{\mu}})\,, \qquad (13)$$

$$V^b_{x,\mu}(l) = \frac{1}{2}\mathrm{tr}(\tau^b\Phi_x^+ U_{x,\mu} \ldots U_{x+(l-1)\hat{\mu},\mu}\Phi_{x+l\hat{\mu}})\,. \qquad (14)$$

Since already the masses of the lowest states in the 2^{++} channel are relatively heavy we have not included Wilson loop contributions here. Therefore, the wave functions of 2^{++} excited states have to be taken with care.

In our procedure, finding the eigenfunctions $\tilde{\Psi}_i^{(n)}$ is tantamount to determine an optimal source operator $\mathcal{O}^{(n)}$ for the eigenstate $|\mathbf{\Psi}^{(n)}\rangle$ as a superposition of the original operators $\mathcal{O}_i$,

$$\mathcal{O}^{(n)} = \sum_{i=1}^{N} \Psi_i^{(n)}\mathcal{O}_i\,, \qquad (15)$$

where the coefficients $\Psi_i^{(n)}$ are related to the normalised solutions $\tilde{\Psi}_i^{(n)}$ of the generalised eigenvalue equation (8) by $\Psi_i^{(n)} = L_{ij}^{T\ -1}\tilde{\Psi}_j^{(n)}/(\mu^{(n)}(t_0, t_0))^{1/2}$. These coefficients define the weight of the chosen operators contributing to $\mathcal{O}^{(n)}$ and express the spatial extendedness of the eigenstate $|\mathbf{\Psi}^{(n)}\rangle$ under study.

In the 1^{--} and 2^{++} channels the index i is used to label the size l of the corresponding Higgs string operator in lattice units. In the case of the 0^{++} channel the label $l = 0$ refers to the operator ρ_x^2, and for $l \geq 1$ we have to distinguish between the $l^{\rm th}$ contribution from Higgs strings and that from Wilson loops.

We have performed simulations using the update algorithms as described in our previous works [3]. In the error analysis of the wavefunctions and masses we have used the jackknife technique. As an example of the outcome of the analysis we show in Fig. 1 the exponential decay of the diagonal elements of the correlation matrix $\mu^{(n)}(t, t_0)$ for the first five states ($n = 1, \ldots, 5$) in the 0^{++} channel as

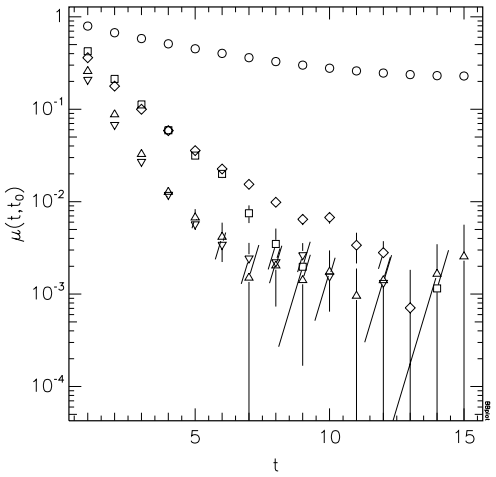

Fig. 1. Example of the exponential decay of $\mu^{(n)}(t,t_0)$ for the five lowest states

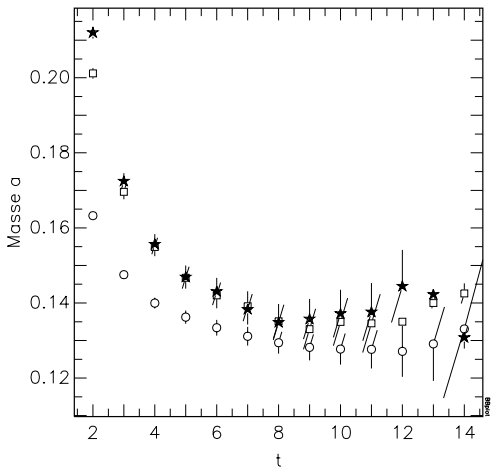

Fig. 2. 0^{++} ground state effective mass obtained from cross correlations ($\circ$), compared to results solely from $S_{x,1}+S_{x,2}$ ($\Box$) and ρ_x^2 ($\star$)

they are found in the symmetric phase (at $\beta_G = 12, \beta_H = 0.3434$) for a Higgs mass of $M_H^* = 70$ GeV. The mass estimates are obtained by fitting $\mu^{(n)}(t,t_0)$, throughout a plateau region of the effective mass, to a hyperbolic cosine form, taking into account the estimated errors of the correlation functions. The improvement achieved by using cross correlations is demonstrated in Fig. 2. As expected, the cross correlation method leads to lower mass values.

The measurements for a Higgs mass $M_H^* = 70$ GeV ($\lambda_3/g_3^2 \approx 0.09570$) were performed below but near to the endpoint of the phase transition. At both sides, in the symmetric and in the Higgs phase, we used a respective line of constant physics corresponding to $m_3^2(g_3^2)/g_4^2 \approx 0.00023$ in the symmetric and $m_3^2(g_3^2)/g_4^2 \approx -0.043$ in the Higgs phase. This corresponds to $T \approx 1.02T_c$ and $T \approx 0.98T_c$, respectively [9,3]. The gauge coupling β_G has been varied from 8 to 16 in order to examine the extrapolation to the continuum. The choice of the actual simulation parameters as near as possible to the phase transition line was dictated by the necessity to avoid tunnelling between the phases. Besides the used lattice size of 30^3 we have additionally investigated the wave functions in the symmetric phase for the 1^{--} and 2^{++} channels on a 50^3 lattice which permitted to increase the range of l in the operator basis. On a lattice of given size, the spatial extension of operators is restricted to half of the lattice size.

Table 1. Used statistics per (β_G, β_H) in the measurements

Phase	Channel	M_H^* GeV	L^3	β_G	independent configurations
symmetric	$1^{--}, 2^{++}$	70	50^3	8,12,16	20000
	$0^{++}, 1^{--}, 2^{++}$	70	30^3	8,12,16	12000
Higgs	0^{++},$1^{--}, 2^{++}$	70	30^3	8,12,16	12000
crossover	0^{++},$1^{--}, 2^{++}$	100	30^3	12	4000

At the larger Higgs mass of $M_H^* = 100$ GeV ($\lambda_3/g_3^2 \approx 0.1953$), above the endpoint of the phase transition [4, 5], we have studied the spectral change with decreasing temperature (increasing β_H), from the "symmetric" to the "Higgs" side of the crossover line, only at one fixed $\beta_G = 12$.

The accumulated statistics of our measurements in the symmetric and Higgs phases as well as in the crossover region for each pair of β_G and β_H values is summarised in Table 1.

By measuring the autocorrelations for the operators of interest we determined the frequency of measurements during the updating in order to retain only independent configurations.

3 Bound states in the symmetric phase at $M_H^* = 70$ GeV

Using the cross correlation technique we were able to obtain the wave function squared corresponding to the optimised operator for each individual state in the spectrum. Being functions of a physical distance, the squared wave functions are shown immediately *vs.* l *a* g_3^2 in order to overlay data from measurements at various gauge couplings (lattice spacings) taken along a line of constant physics.

The results for the 0^{++} channel are collected in Figs. 3-5 for the squared wave functions. The contributions from the Higgs string and Wilson loop operators are shown separately in order to identify clearly Higgs and W-ball excitations. We observe no mixing of these two operator types in the Higgs ground state and the first excitation. The second excited state in this channel consists of a pure excitation of gauge degrees of freedom (d.o.f.) and can be identified with a W-ball in analogy with the glueballs of pure $SU(2)$. Our results on this decoupling confirm the

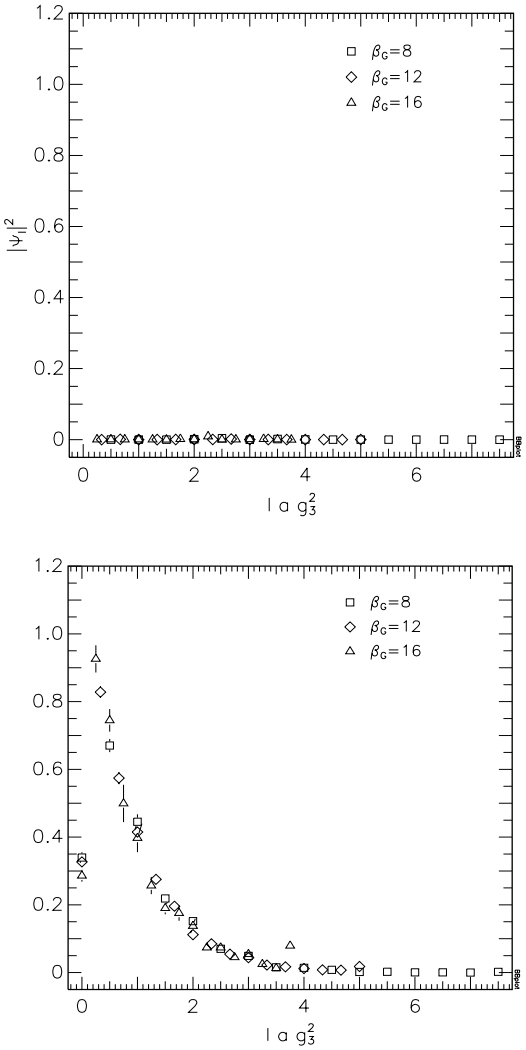

Fig. 3. Squared wave function of the ground state in the 0^{++} channel, measured on a 30^3 lattice in the symmetric phase; upper: $W_{x,1,2}(l) + W_{x,2,1}(l)$, lower: $S_{x,1}(l) + S_{x,2}(l)$; $l = 0, \ldots, 15$

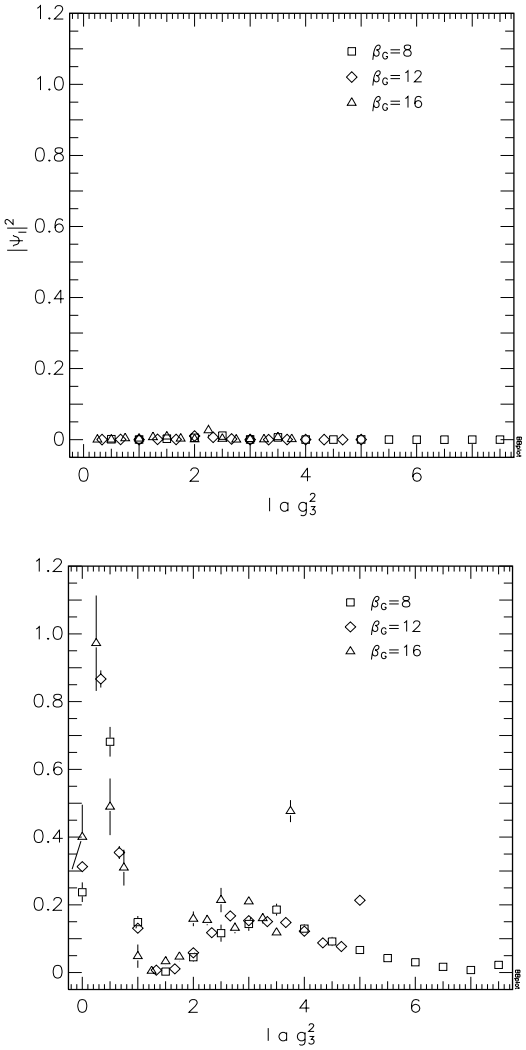

Fig. 4. Same as Fig. 3 for the first excited state

observations in [16] made at a much lighter Higgs mass in the symmetric phase near to the strongly first order phase transition.

The squared wave functions for ground and excited states in the 1^{--} and 2^{++} channels are presented in Fig. 6 and 7.

At this point it is due to come back to the issues of completeness (of the operator set) and orthogonality (of the states $\Psi_i^{(n)}$). We have already noticed that the eigenvectors of (7) become orthogonal only in the limit of a complete operator set, and that the scalar product between different states should be used to examine the degree of completeness. This test shows what are the difficulties in practice. We have studied the scalar product between the ground state and the first excitation as a function of the maximal length l_{max} of the operator set $S_{x,\mu}(l)$ by gradually clipping the set of operators from l_{max}=25 (on the 50^3 lattice) down to zero. One would expect that this function tends to zero for $l_{max} \to \infty$. Actually the scalar product reaches a minimum at some finite l_{max} and starts to grow at bigger maximal length due to statistical and numerical errors in the case of larger operators and matrices.

Inspecting the wave function of the ground state in the 1^{--} channel we observe that for very large operators the contribution to this state vanishes. This is true to a high accuracy for the largest physical volume that we have considered, at $\beta_G = 8$. If we chose higher β_G (smaller volumes) along the line of constant physics (in order to explore the approach to the continuum) the operator set in use with fixed $l_{max} = L/2$ does not describe anymore the whole wave function. There are fake contributions accumulating in the contribution of the longest operator in the set which, in principle, belong to more extended operators which are not included. A similar behaviour can be observed for the excited states if one compares the wave functions varying the operator set. For the second excited state shown in Fig. 6 it is clearly seen that in the case

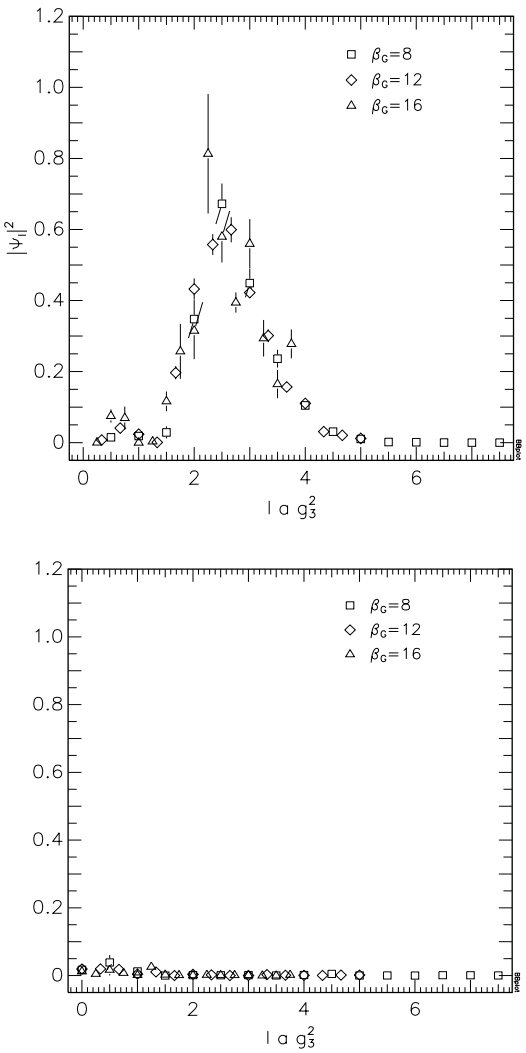

Fig. 5. Same as Fig. 3 for the second excited state

of β_G=16 (small physical volume) this state is not satisfactorily described by the limited operator basis. An optimal continuum limit for the wave function would require to choose the same maximal operator length in physical units, *i.e.* doubling the length in lattice units when one goes over from $\beta_G = 8$ to $\beta_G = 16$. This is, however, difficult to accomplish with restricted resources, not only because of the lattice size. Larger cross correlation matrices would additionally require larger statistics to get stable results from the diagonalisation procedure.

Considering only wave function data obtained at fixed β_G (tolerating a non-perfect overlay of data from different a in a physical scale) the presented figures illustrate perfectly that the number of zeroes of the wave functions corresponds to the level of excitation (knot rule).

Due to the mentioned difficulties, it becomes more and more difficult to extract the masses of higher excitations, in particular if already the ground state is very heavy and if the lattice becomes dangerously small (when we attempt to study the continuum limit) compared to the physical

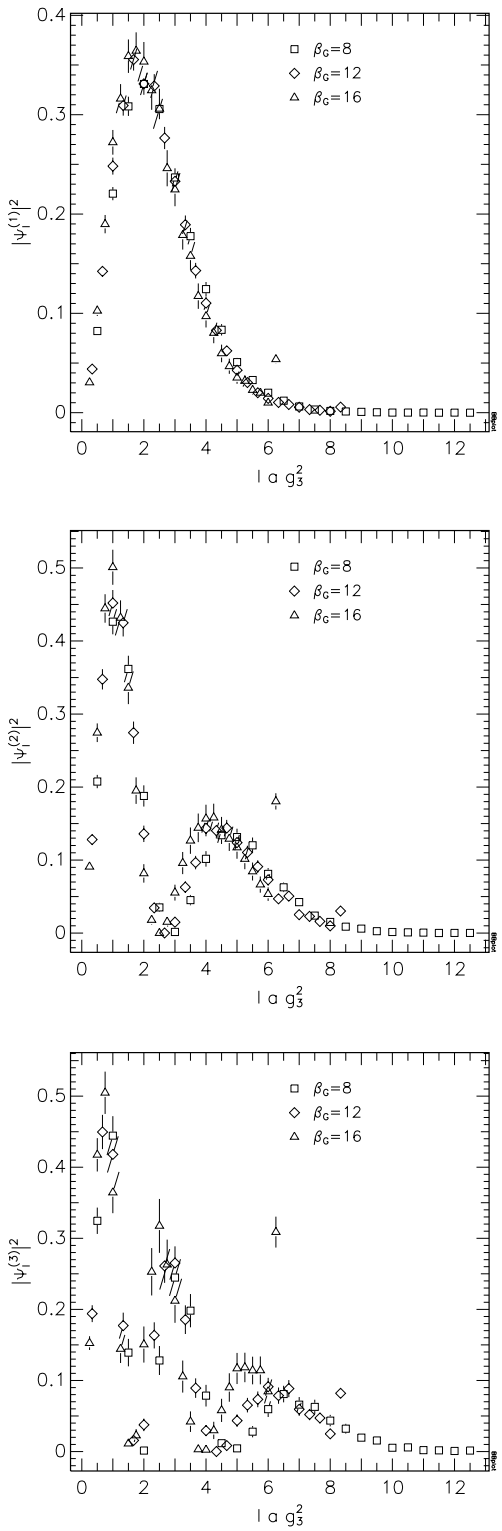

Fig. 6. Squared wave function in the 1^{--} channel, measured on a 50^3 lattice in the symmetric phase; ground state and two excited states

extension of the wave function corresponding to the state under discussion.

For the ground states we are now able to reexamine our previous spectrum investigations [3] where we measured

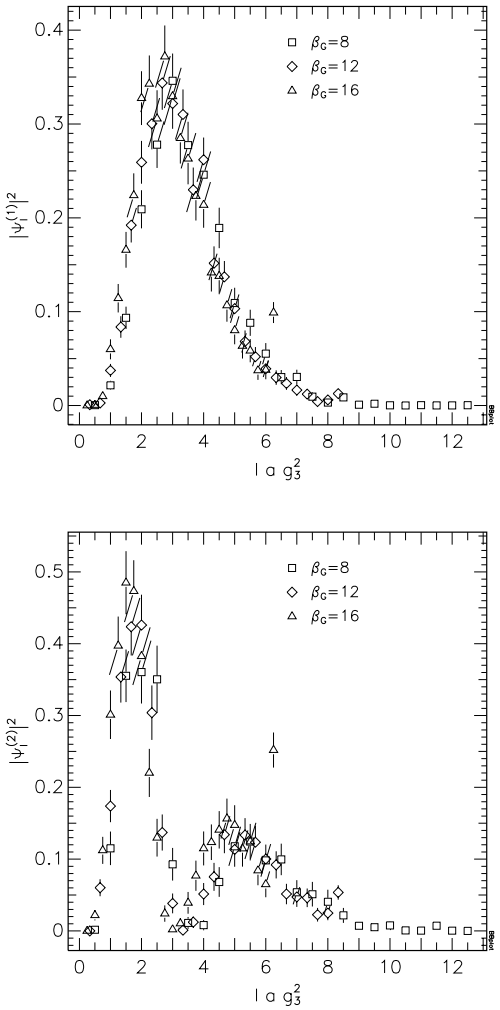

Fig. 7. Squared wave function in the 2^{++} channel, measured on a 50^3 lattice in the symmetric phase; ground state and first excited state

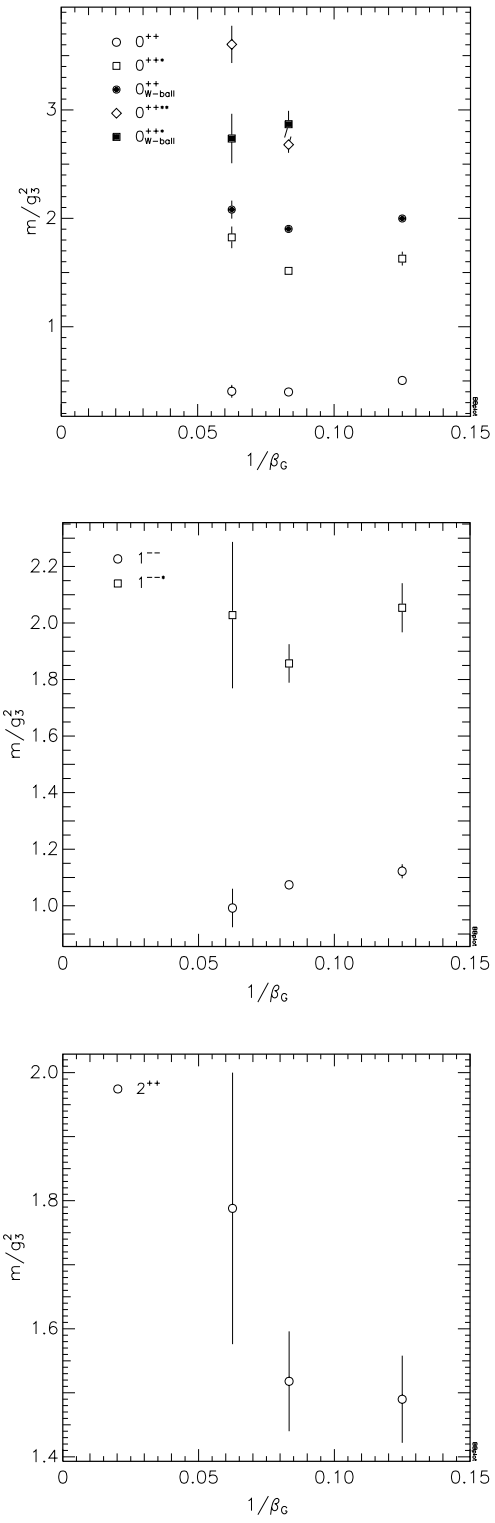

Fig. 8. Mass spectrum in the symmetric phase as function of $1/\beta_G$

the mass without use of the cross correlation technique. In the 0^{++} channel the agreement is satisfactory since the ground state wave function is well dominated by the shortest operators like $(1/2)\mathrm{tr}(\Phi_x^+ U_{x,\mu}\Phi_{x+\hat{\mu}})$. Mass measurements in the 2^{++} channel and for the W-ball states have proved to be difficult in our previous studies, and we did not report on that in [3]. From the present analysis we recognise that this difficulty is related to the large spatial extendedness of these states.

Using the cross correlation technique we have found in the symmetric phase the ground state mass and the first excitations. We restricted ourselves to an identification only of those masses with a still reasonable plateau behaviour and a not too large mass value in lattice units. Notice that the operators are classified in the angular momentum J only modulo 4; therefore we cannot exclude that states with higher masses have got contributions from states with higher J.

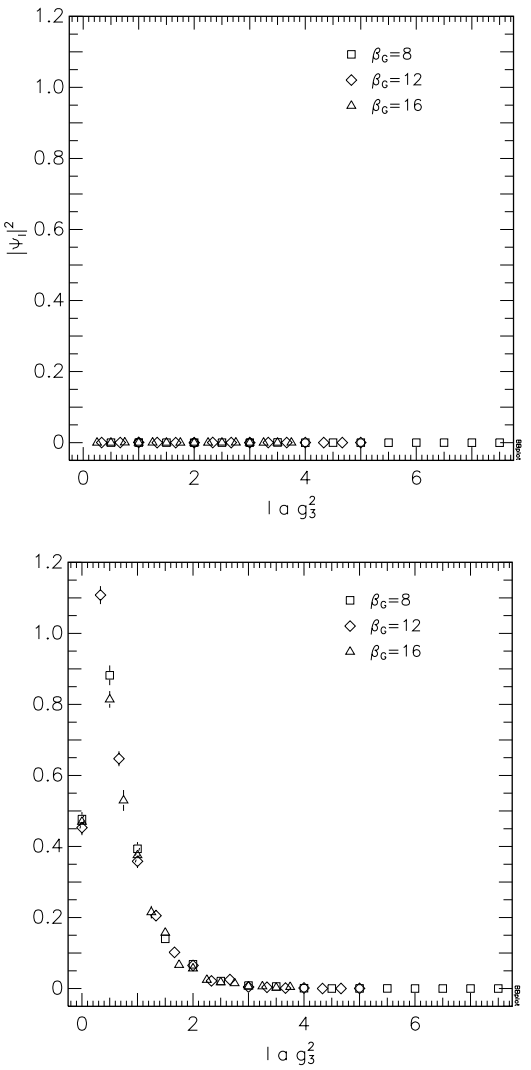

Fig. 9. Squared wave function of the ground state in the 0^{++} channel, measured on a 30^3 lattice in the Higgs phase; lower: $W_{x,1,2}(l) + W_{x,2,1}(l)$, upper: $S_{x,1}(l) + S_{x,2}(l)$; $l = 0, \ldots, 15$

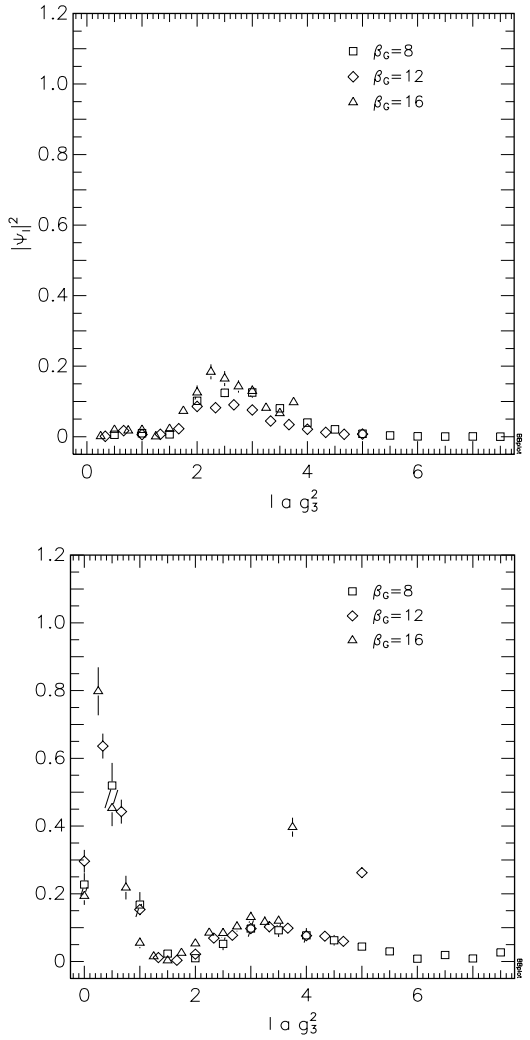

Fig. 10. Same as Fig. 9 for the first excited state

The masses of the first excitations in the symmetric phase (for 2^{++} only of the lowest state) are presented in Fig. 8 and the fitted masses are collected in Tables 9-10 of Appendix B.

We tried to illustrate whether an approach to the continuum limit is already indicated by the present measurements. The big errors of the excited state in the 1^{--} channel and, even more, of the ground state in the 2^{++} channel show where the problems are.

Concluding this section we would like to stress that qualitatively there is no difference in the spectrum on the high temperature side of the phase transition for light or relatively heavy Higgs masses as long as the phase transition persists. The gauge d.o.f. decouple from the Higgs excitations and form W-balls similar to confined $3D$ pure $SU(2)$ gauge theory [21].

4 The spectrum in the Higgs phase near to the endpoint of the transition

On the Higgs side of the phase transition pure gauge matter (W-ball) excitations are not expected to be present in the spectrum. This hypothesis has been numerically verified at light Higgs masses [16]. Now, at $M_H^* = 70$, we observe in the Higgs phase near to the transition the following. In the 1^{--} and 2^{++} channels the spectrum looks similar to that in the symmetric phase. This was expected from earlier studies for the 1^{--} channel. Therefore the squared wave functions are not shown explicitly.

Note, that in the 2^{++} channel we have not used operators with pure gauge degrees of freedom. Therefore, we cannot observe the expected difference for 2^{++} W-balls.[2]

In the 0^{++} channel, however, our operator set is sufficient to observe a marked difference between the phases which is not in accordance to naive expectations. As a characteristic feature we observe the mixing between the two operator types, W-ball operators (pure gauge d.o.f.)

[2] Results for the W-balls with $J = 2$ can be found in [17].

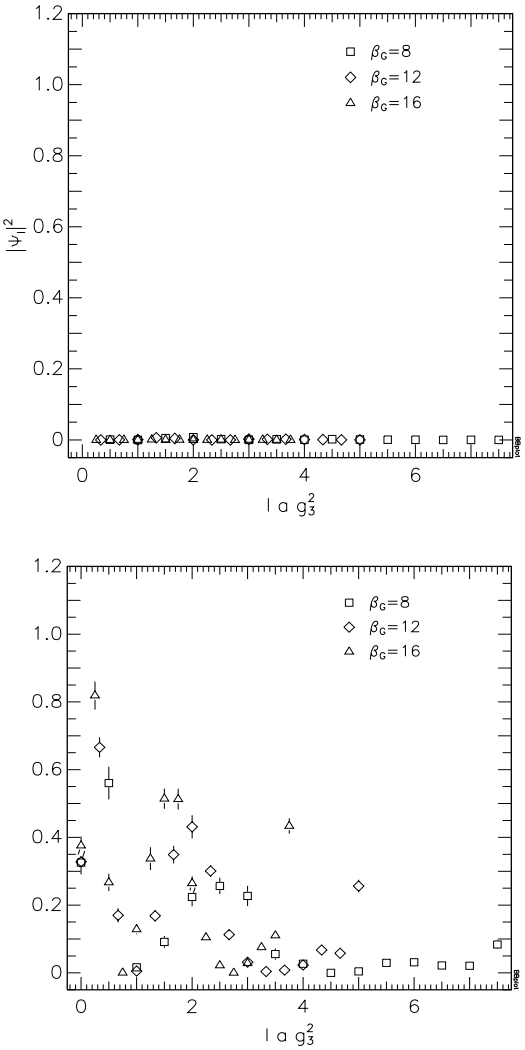

Fig. 11. Same as Fig. 9 for the second excited state

and operators projecting onto Higgs states. The squared ground state wave function looks similar to that in the symmetric phase, contributions from Wilson loops to the operator projecting onto the lowest mass states are absent (Fig. 9).

However, already the first excited Higgs state contains a noticeable contribution from Wilson loop operators of almost 20 percent (Fig. 10). Earlier measurements at a Higgs mass of $M_H^* = 35$ GeV [17] (where the phase transition is very strong) did not indicate such a mixing. We interpret this mixing of Higgs and gauge d.o.f. as a signal of the near endpoint of the phase transition. Deeper in the Higgs phase the contribution from gauge degrees of freedom is expected to disappear also at this high Higgs mass. This tendency has been checked in our simulations at $M_H^* = 100$ GeV to be discussed in the next section. This suggests a scenario according to which the first and second excited states present on the symmetric side (Higgs and W-ball, respectively) merge into one common state on the Higgs side. The remaining gauge degrees of freedom

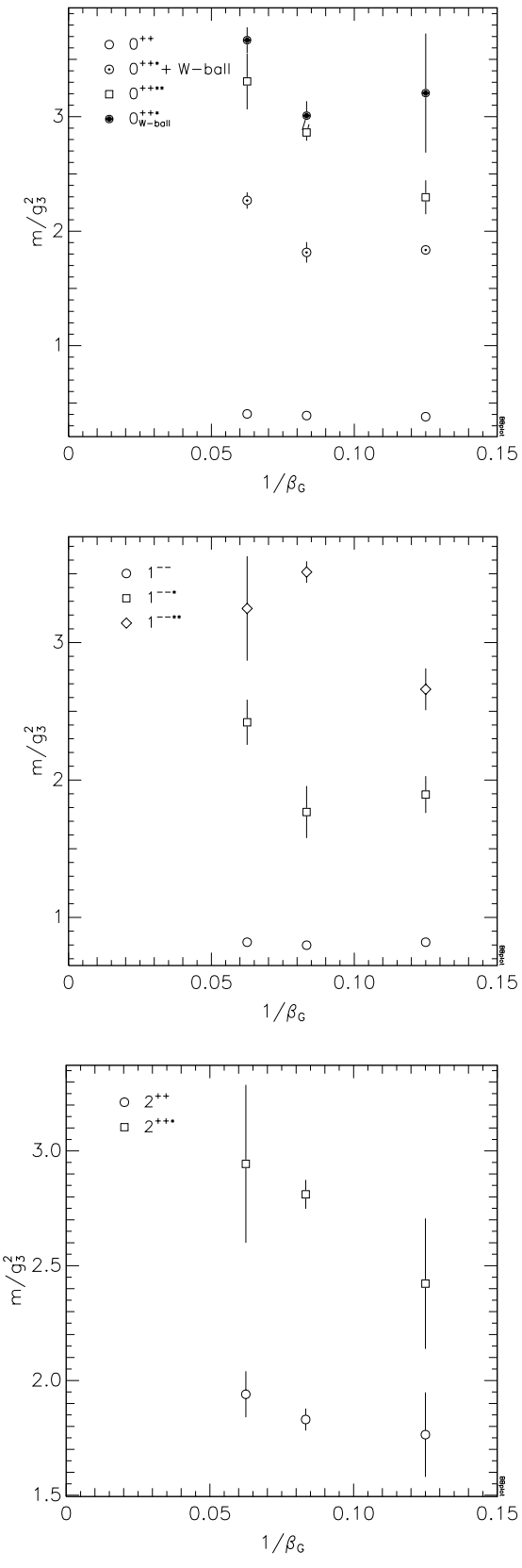

Fig. 12. Mass spectrum in the Higgs phase as function of $1/\beta_G$

are fading away from that state with further lowering of temperature (increasing β_H).

The second excited state in the 0^{++} channel on the Higgs side (Fig. 11) is qualitatively a state with Higgs excitations (no W-ball contributions) followed by a third excited state which looks dominantly like a W-ball.[3]

In Fig. 12 our results for the masses at three different gauge couplings on a line of constant physics are collected, the corresponding values can be found in Tables 11 and 12. Similar as before, the lowest mass state has a reasonable continuum limit whereas with increasing mass the accuracy rapidly deteriorates and an extrapolation to vanishing lattice spacing becomes difficult.

5 The spectral change at the rapid crossover for $M_H^* = 100$ GeV

We have noticed that the spectra of the two phases differ mainly with respect to the contributions of the Wilson loops (gauge d.o.f.) to the excited states in different channels. Therefore we study this change in more detail while *continuously* passing the crossover line (changing the hopping parameter β_H) at fixed gauge coupling $\beta_G = 12$. Sufficiently above the phase transition endpoint (for large enough scalar self-couplings) no large autocorrelation times are expected which would prevent us to cross that region of still rapidly changing thermodynamical observables and to determine the physical excitations. As long as a true phase transition exists, due to tunnelling one would measure in the 0^{++} channel not the actual lowest mass in the spectrum related to the respective phases but rather a characteristic correlation length characterising the transition itself.

Our simulation have been performed at a scalar–gauge coupling ratio $\lambda_3/g_3^2 \approx 0.1953$ corresponding to the approximate Higgs mass parameter $M_H^* = 100$ GeV. We have used the same operator set as in the previous analysis. The statistics of 4000 independent configurations per β_H value limits the capability to analyse higher excitations. Nevertheless, we found a behaviour very similar to our results obtained at $M_H^* = 70$ GeV. The results on the masses are collected in Tables 13 and 14.

The similarities concern both the high temperature side of the crossover (where one expects thermodynamic properties being close to those of the symmetric phase at smaller Higgs mass) and the region very near to the crossover line on the so-called Higgs side of the crossover (resembling the Higgs phase at slightly lower Higgs mass). In Figs. 13 we present the spectrum of the lowest states in the 0^{++}, 1^{--} and 2^{++} channels as function of $m_3^2(g_3^2)/g_3^4$ (or β_H) over a wide interval above and below the crossover (*i. e.* in temperature).

By inspecting these Figures we localize the crossover at $m_3^2(g_3^2)/g_3^4 \approx -0.05$. Of particular interest for us is to study the mixing of Higgs and gauge degrees of freedom in the 0^{++} channel. Looking at the excited states in this channel of Figs. 13 we conclude that the scalar

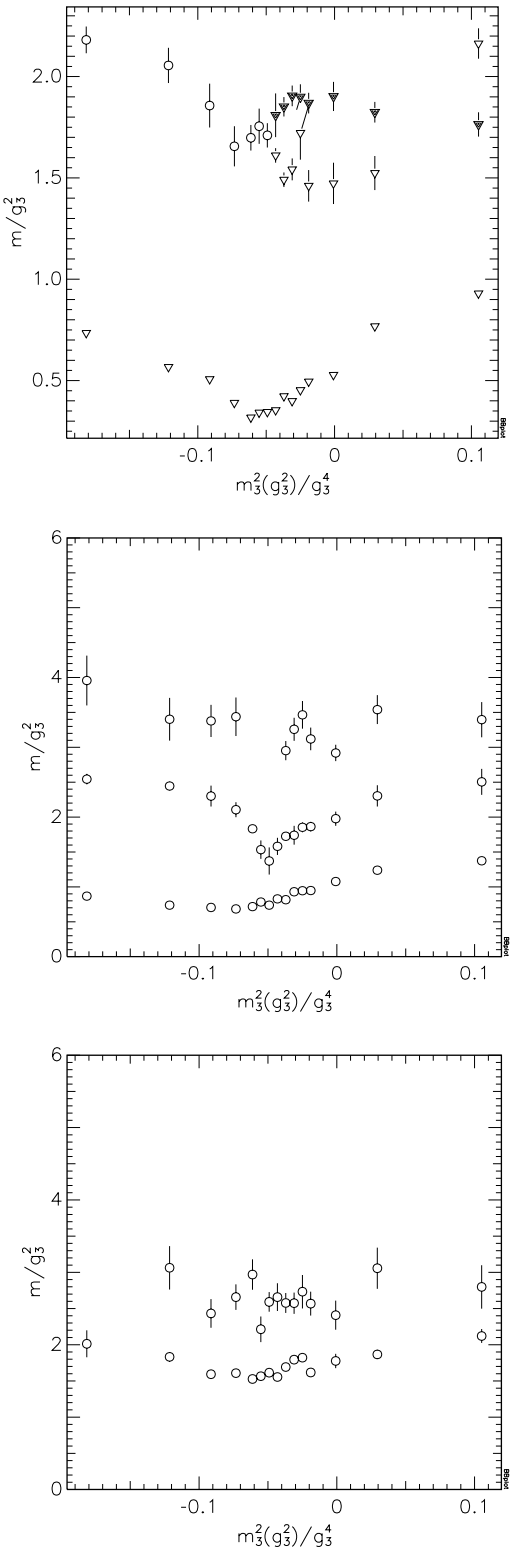

Fig. 13. Spectra near the crossover in the channels 0^{++}, 1^{--} and 2^{++}; in the 0^{++} channel open triangles denote Higgs states, full triangles W-ball states and open circles Higgs states with an admixture of excited gauge d.o.f.

[3] Its wave function is not shown here.

and gauge sector are approximately decoupled as long as one keeps away from the crossover line on the high temperature side. This has already emphasised in [16,17] where cases of smaller (characterized by the existence of a strong first order phase transition) and larger Higgs self-couplings (far above the endpoint of the phase transition) have been studied. The mass of the lowest W-ball state (full triangle) is roughly independent of β_H as long as one does not come too close to the crossover. Thus, on the high temperature side of the crossover, the ordering of states qualitatively resembles the spectrum at smaller values of Higgs self-coupling (at $M_H^* = 70$). If one approaches the crossover temperature the mass of the first (Higgs-like) excitation is moving up towards the lowest W-ball state whose mass decreases. At some point we observe a growing admixture to the Higgs excitation by contributions from Wilson loop operators which reaches about 17 %. Then the wave function of the remaining state looks similar to Fig. 10. At higher β_H (lower temperature, deeper in the would-be Higgs phase) the admixture from pure gauge d.o.f. disappears again from this state. This has been explicitly checked for the first excited state in the 0^{++} channel corresponding to the data point at $\beta_H = 0.37, m_3^2(g_3^2)/g_3^4 \approx -3.4$ in Table 13 (far on the Higgs-side) where we did not observe any contribution from Wilson loops.

6 Summary and conclusions

In this paper we complemented our numerical study of the electroweak phase transition using the $3D$ $SU(2)$–Higgs model by an investigation of the ground state and some excited states in three J^{PC} channels. Our interest was focused on Higgs screening masses slightly below and above the end of the first order phase transition where we wanted to understand the qualitative relations between the higher and lower temperature regions. This investigation was done with the help of cross correlation matrix functions between different operators with the same quantum numbers. We were able significantly to improve the old ground state mass estimates which were obtained just by fitting a single correlation function over the plateau region of the effective mass. In our earlier work, the proper extension of the operators had been selected by hand, according to a signal *vs.* noise criterion for various *diagonal* correlators. Implicitly this procedure, too, gives some information concerning the best-projecting operator that relates the vacuum state to the lowest mass bound state in the given channel. Today, many techniques are known allowing to construct source operators with improved projection properties. For the $SU(2)$–Higgs and the pure $SU(2)$ model these are smearing techniques which were investigated and used in our present context in [20,16,17]. These improved operators take the extended character of the states into account, too, although in a summary way.

Using the cross correlation technique the extended character can be specified in a more detailed and systematic way. Within a preselected set of operators, the method finds the projection strength of a each operator onto the first few states with quantum numbers compatible to the operators admitted. The result can be represented as a wavefunction. Moreover, different Fock space components (Higgs bound states and gauge-ball states) can be treated in parallel. In the present paper this feature has been proven essential for the understanding of excited states and to point out similarities and differences between neighbouring regions of the extended phase diagram. Our operators were classified in a very simple way (extended Higgs strings and Wilson loops without internal structure) with a clear reference to the corresponding length in lattice units. This would allow us to interpret the results in terms of a configuration space wave function. Anticipating this possibility and just to make the first step, our operator choice was the simplest one to incorporate the notion of spatial extension. It was possible to see the particular effects that generically occur when the admitted operator set becomes too small (in attempts to go too far towards the continuum limit $a \to 0$) to cover the state under discussion. The continuum limit of the screening masses and wave functions has to be accompanied by correspondingly larger lattices with the same physical volume. But then, simply increasing the operator set simultaneously, would require much higher statistics to reach the necessary accuracy and stability in the diagonalisation procedure. This is a reason to include, in a next step of improvement of the method, smearing of the fields entering the operators and/or the construction of blocked operators.

Our first measurements presented here were done at a Higgs mass of $M_H^* = 70$ GeV, near to but still below the endpoint of the transition. We found that the physics at this point is already influenced by the endpoint. The W-ball states characteristic for the symmetric phase do not disappear in the Higgs phase as long as one keeps near to the transition line. However, the first W-ball state appears here as an admixture to the first excited Higgs state. A second W-ball state could also be seen in the Higgs phase very near to the phase transition.

Our measurements in the crossover region have shown that also there the W-ball state will finally disappear deeper on the low temperature side of the crossover. In our simulations at $M_H^* = 100\,\mathrm{GeV}$ we could study the mixing of the first W-ball with the first Higgs excited state, both being well separated on the symmetric side of the crossover (similar to the symmetric phase at lower Higgs mass), in some detail by continuously monitoring the spectral evolution across the crossover line. Over most of the parameter space on the high temperature side of the crossover region, however, decoupling of the gauge and scalar sector has been established.

Appendix A
Angular momentum in 2+1 dimensions

Gauge invariant operators can be constructed in the $3D$ $SU(2)$–Higgs model and can be used to define states and wave functions. They are classified with respect to the

Table 2. Symmetry transformations of $\mathcal{D}_4$ group

$C(n_C)$		angle
$\mathbf{1}(1)$	Identity	
$C_4^2(1)$	rotation (0,0)	$\phi = \pi$
$C_4(2)$	rotation (0,0)	$\phi = \pi/2$
$C_2(2)$	reflection x, y	
$C_2'(2)$	reflection diagonal	

Table 3. Characters χ^J of full $SO(2)$ symmetry ($C(\phi)$) including reflections (σ_v) for various angular momenta J

$C_\infty \backslash J$	0	1	2	3	4
$\mathbf{1}$	1	2	2	2	2
$C(\phi)$	1	2cosϕ	2cos2ϕ	2cos3ϕ	2cos4ϕ
σ_v	1	0	0	0	0

quantum numbers angular momentum J, parity P and charge conjugation C. While the classification according to C and P is trivial (the eigenvalues of C and P have the same sign for operators which live in the same $x-y$-plane in $2+1$ dimensions) the classification according to J requires some care due to the discreteness of the rotation group. The results are known, we collect here the main results for the convenience of the reader and to apply them to the operators of interest. For the $3+1$ dimensional case the classification can be found in [22,23]. Some of the results are already described in [24], we follow the description in [25].

To define the angular momentum of a given operator on the lattice the transformation properties with respect to the discrete lattice symmetries have to be studied. In our case the continuous symmetry group is $SO(2)$ which gets restored in the continuum limit. In that case the angular momentum is represented by the irreducible representations (IR) of $SO(2)$. On the cubic lattice the group of two-dimensional rotations and reflections is the dihedral group $\mathcal{D}_4$. This group is non-Abelian and has 8 elements ($d = 8$) and 5 irreducible representations. The conjugation classes C with their number of elements n_C and the symmetry transformations are collected in Table 2. The corresponding IR's of $\mathcal{D}_4$ are denoted by A_1, A_2, B_1, B_2 and E, the first four are one-dimensional, the last one has dimension 2.

The characters of $\mathcal{D}_4$ are computed by reducing the characters of the full $SO(2)$ group (including reflections) (Table 3) to those of the subduced representation D_0^J by taking the discrete angles of Table 2. The result is shown in Table 4.

The characters of the conjugation classes of $\mathcal{D}_4$ in the IR of this group are taken from the character table of [25] and are shown in Table 5. Using the characters given in Tables 4 and 5 we can compute the multiplicities for the

Table 4. Characters χ_C^J of conjugation classes C in the subduced representation D_0^J

$C\backslash J$	0	1	2	3	4
$\mathbf{1}(1)$	1	2	2	2	2
$C_4^2(1)$	1	-2	2	-2	2
$C_4(2)$	1	0	-2	0	2
$C_2(2)$	1	0	0	0	0
$C_2'(2)$	1	0	0	0	0

Table 5. Characters χ_C^{IR} of the conjugation class C in the IR of $\mathcal{D}_4$

$C\backslash IR$	A_1	A_2	B_1	B_2	E
$\mathbf{1}(1)$	1	1	1	1	2
$C_4^2(1)$	1	1	1	1	-2
$C_4(2)$	1	1	-1	-1	0
$C_2(2)$	1	-1	1	-1	0
$C_2'(2)$	1	-1	-1	1	0

Table 6. Multiplicities m_J^{IR} of IR of $\mathcal{D}_4$ in the subduced representation D_0^J for angular momentum J

$J\backslash IR$	A_1	A_2	B_1	B_2	E
0	1	0	0	0	0
1	0	0	0	0	1
2	0	0	1	1	0
3	0	0	0	0	1
4	1	1	0	0	0

IR of the dihedral group $\mathcal{D}_4$ for angular momentum J:

$$m_J^{IR} = \frac{1}{d} \sum_C n_C \chi_C^{IR} \chi_C^J \,, \tag{16}$$

they are shown in Table 6.

The multiplicities for a given operator are obtained by inspecting its properties under those discrete transformations. The extended operators (given in (13)) transform as vectors with positive parity ($S_{x,\mu}(l)$) or with negative parity ($V^b_{x,\mu}(l)$). The characters and the multiplicities are shown in Table 7. We observe that the operator $S_{x,\mu}(l)$ transforms simultaneously under the IR A_1 and B_1, whereas $V^b_{x,\mu}(l)$ transforms with E only.

Using a projection operator P^{IR} one is able to project onto *one* irreducible representation in the case of $S_{x,\mu}(l)$. A projection operator for a given IR is constructed as the sum over all conjugation classes C weighted by the character χ_C^{IR} for that IR (Table 5):

Table 7. Characters and multiplicities for the operators $S_{x,\mu}(l)$ and $V^b_{x,\mu}(l)$

χ^{IR}_C	$\mathbf{1}(1)$	$C^2_4(1)$	$C_4(2)$	$C_2(2)$	$C'_2(2)$
$S_{x,\mu}(l)$	2	2	0	2	0
$V^b_{x,\mu}(l)$	2	-2	0	0	0
m^R_J	A_1	A_2	B_1	B_2	E
$S_{x,\mu}(l)$	1	0	1	0	0
$V^b_{x,\mu}(l)$	0	0	0	0	1

Table 8. Quantum numbers and gauge invariant lattice operators

0^{++}:	$S_{x,1}(l) + S_{x,2}(l)$
	$W_{x,1,2}(l) + W_{y,1,2}(l)$
1^{--}:	$V^b_{x,1}(l) + V^b_{x,2}(l)$
2^{++}:	$S_{x,1}(l) - S_{x,2}(l)$
	$W_{x,1,2}(l) - W_{y,1,2}(l)$

$$P^{IR} = \sum_C \chi^{IR}_C C\,. \tag{17}$$

The C have to be taken in a matrix representation taking into account parity.

For the operator $S_{x,\mu}(l)$ the projection matrices can be used in the form:

$$P^{A_1} = 4\begin{pmatrix} 1 & 1 \\ 1 & 1 \end{pmatrix}, \quad P^{B_1} = 4\begin{pmatrix} 1 & -1 \\ -1 & 1 \end{pmatrix}. \tag{18}$$

From here the fixed angular momenta of the operators to be used are defined as shown in Table 8. It is obvious from Table 6 that all operators describing a $J = 0$ angular momentum state also overlap to a $J = 4$ state. These higher states are expected to be sufficiently heavier than the lightest $J = 0$ state. Similarly this also holds for the other operators. Thus for the cubic lattice only operators with $J(\mathrm{mod}\ 4)$ can be constructed what restricts the identification of highly excited states in the channels discussed here.

Appendix B
Tables of masses for ground states and excitations

Table 9. Masses of 0^{++} states in units of g_3^2 at $M_H^* = 70$ GeV in the symmetric phase (30^3 lattice)

β_G	β_H	0^{++}	0^{++*}	$0^{++}_{\mathrm{W-ball}}$	0^{++**}	$0^{++*}_{\mathrm{W-ball}}$
8	0.3490	0.504(16)	1.628(64)	1.998(37)		
12	0.3434	0.398(18)	1.515(33)	1.902(26)	2.679(75)	2.868(123)
16	0.3407	0.404(59)	1.824(100)	2.080(83)	3.604(172)	2.736(228)

Table 10. Masses of 1^{--} and 2^{++} states in units of g_3^2 at $M_H^* = 70$ GeV in the symmetric phase (30^3 lattice)

β_G	β_H	1^{--}	1^{--*}	2^{++}
8	0.3490	1.122(35)	2.054(87)	1.498(68)
12	0.3434	1.074(14)	1.857(68)	1.518(78)
16	0.3407	0.992(68)	2.028(259)	1.788(21)

Table 11. Masses of 0^{++} states in units of g_3^2 at $M_H^* = 70$ GeV in the Higgs phase (30^3 lattice)

β_G	β_H	0^{++}	0^{++*} + gauge d.o.f.	$0^{++}_{\mathrm{W-ball}}$	0^{++**}
8	0.34970	0.380(4)	1.836(36)	2.296(148)	3.206(519)
12	0.34368	0.390(3)	1.815(90)	2.862(71)	3.009(126)
16	0.34088	0.404(4)	2.268(71)	3.308(244)	3.668(112)

Table 12. Masses of 1^{--} and 2^{++} states in units of g_3^2 at $M_H^* = 70$ GeV in the Higgs phase (30^3 lattice)

β_G	β_H	1^{--}	1^{--*}	2^{++}	2^{++*}
8	0.34970	0.820(8)	1.894(134)	1.764(184)	2.422(288)
12	0.34368	0.798(6)	1.767(189)	1.830(48)	2.811(63)
16	0.34088	0.820(12)	2.420(151)	1.940(100)	2.944(344)

Table 13. Masses of 0^{++} states in units of g_3^2 at $M_H^* = 100$ GeV (crossover region) depending on β_H

	β_H	0^{++}	0^{++*}	$0^{++}_{\mathrm{W-ball}}$
symmetric	0.34200	2.037(51)	3.330(225)	1.770(59)
	0.34510	0.930(18)	2.163(75)	1.764(59)
	0.34560	0.768(12)	1.525(84)	1.824(51)
	0.34580	0.528(14)	1.473(102)	1.902(71)
	0.34592	0.495(14)	1.461(78)	1.869(51)
	0.34596	0.453(14)	1.722(131)	1.899(63)
	0.34600	0.399(53)	1.542(53)	1.905(51)
	0.34604	0.423(14)	1.491(35)	1.851(48)
	0.34608	0.354(12)	1.611(35)	1.809(107)
		0^{++}	0^{++*} + gauge d.o.f.	
	0.34612	0.345(6)	1.710(60)	
	0.34616	0.342(12)	1.755(87)	
	0.34620	0.318(7)	1.698(63)	
	0.34628	0.390(6)	1.656(99)	
	0.34640	0.507(6)	1.857(108)	
	0.34660	0.567(12)	2.055(87)	
	0.34700	0.735(9)	2.181(66)	
		0^{++}	0^{++*}	
Higgs	0.37000	2.723(48)	5.250(339)	

Table 14. Masses of 1^{--} and 2^{++} states in units of g_3^2 at $M_H^* = 100$ GeV (crossover region) depending on β_H

	β_H	1^{--}	1^{--*}	1^{--**}	2^{++}	2^{++*}
symmetric	0.34200	3.261(177)			3.255(84)	
	0.34510	1.374(48)	2.505(185)	3.396(252)	2.121(96)	2.799(300)
	0.34560	1.239(30)	2.304(152)	3.540(206)	1.866(63)	3.057(284)
	0.34580	1.077(14)	1.977(102)	2.919(116)	1.776(98)	2.409(201)
	0.34592	0.948(21)	1.863(68)	3.120(162)	1.670(35)	2.568(164)
	0.34596	0.945(21)	1.854(71)	3.465(197)	1.821(53)	2.733(231)
	0.34600	0.930(12)	1.740(135)	3.258(164)	1.794(51)	2.574(147)
	0.34604	0.816(35)	1.725(59)	2.952(137)	1.692(45)	2.577(137)
	0.34608	0.828(26)	1.581(123)		1.554(51)	2.658(192)
	0.34612	0.738(24)	1.371(194)		1.614(29)	2.592(135)
	0.34616	0.783(17)	1.533(132)		1.566(42)	2.214(177)
	0.34620	0.717(32)	1.833(60)		1.527(42)	2.970(210)
	0.34628	0.684(21)	2.106(107)	3.438(275)	1.608(44)	2.658(177)
	0.34640	0.705(26)	2.301(150)	3.378(231)	1.593(56)	2.433(197)
	0.34660	0.738(24)	2.445(63)	3.402(305)	1.833(65)	3.063(300)
	0.34700	0.867(12)	2.544(75)	3.957(357)	2.013(185)	
Higgs	0.37000	2.400(33)				

References

1. K. Kajantie et al., Nucl. Phys. B **442**, 317 (1995); B **466**, 189 (1996)
2. F. Karsch et al., Nucl. Phys. B **474**, 217 (1996)
3. M. Gürtler et al., Nucl. Phys. B **483**, 383 (1997)
4. K. Kajantie, M. Laine, K. Rummukainen, M. Shaposhnikov, Phys. Rev. Lett. **77**, 2887 (1996)
5. M. Gürtler, E.-M. Ilgenfritz, A. Schiller, Phys. Rev. D **56**, 3888 (1997)
6. M. Gürtler, E.-M. Ilgenfritz, A. Schiller, Eur. Phys. J. C **1**, 363 (1998)
7. Z. Fodor et al., Nucl. Phys. B **439**, 147 (1995); F. Csikor et al., Nucl. Phys. B **474**, 421 (1996); Y. Aoki, Phys. Rev. D **56** 3860 (1997); F. Csikor, Z. Fodor, J. Heitger, Nucl. Phys. B (Proc. Suppl.) **63**, 569 (1998)
8. K. Rummukainen, Nucl. Phys. B (Proc. Suppl.) **53**, 30 (1997)
9. K. Kajantie, M. Laine, K. Rummukainen, M. Shaposhnikov, Nucl. Phys. B **458**, 90 (1996)
10. M. Laine, Nucl. Phys B **451**, 484 (1995)
11. K. Rummukainen et al., preprint CERN-TH-98-08, hep-lat/9805013
12. S. de Jong in *"Higgs Searches at LEP"*, Review talk delivered at the XXXIIIrd Rencontres de Moriond, Les Arcs, France, March 14 – 21 (1998)
13. M. Laine K. Rummukainen, Phys. Rev. Lett. **80** 5259 (1998); CERN-TH-98-122, hep-lat/9804019
14. M.N. Chernodub, F. V. Gubarev, E.-M. Ilgenfritz, A. Schiller, Phys. Lett. B **432**, 83 (1998); ITEP-TH-36/98, KANAZAWA-98-08 and UL-NTZ 30/98 preprint, hep-lat/9807016
15. M. Gürtler, E.-M. Ilgenfritz, A. Schiller, C. Strecha, Nucl. Phys. B (Proc. Suppl.) **63**, 563 (1998), in: "Theory of Elementary Particles, Proceedings of the 31st International Symposium Ahrenshoop, September 2-6, 1997, Buckow/Germany", H. Dorn, D. Lüst. G. Weigt (Editors), Weinheim: Wiley-VCH 1998, p. 253
16. O. Philipsen, M. Teper, H. Wittig, Nucl. Phys. B **469**, 445 (1996)
17. O. Philipsen, M. Teper, H. Wittig, Nucl. Phys. B **528**, 379 (1998)
18. M. Lüscher, U. Wolff, Nucl. Phys. B **339**, 222 (1990)
19. C.R. Gattringer, C.B. Lang, Nucl. Phys. B **391**, 463 (1993)
20. M. Teper: Phys. Lett. B **187**, 345 (1987)
21. M. Teper, Phys. Lett. B **311**, 223 (1993)
22. B. Berg, A. Billoire, Nucl. Phys. B **221**, 109 (1983); K. Ishikawa, G. Schierholz, M. Teper, Z. Phys. C **19** 327 (1983)
23. H.G. Evertz, "Gitteranalyse des Higgs–Mechanismus", Dissertation TH Aachen RX-1200 (1987)
24. V. Agostini, G. Carlino, M. Caselle, M. Hasenbusch, Nucl. Phys. B **484**, 331 (1997)
25. M. Hamermesh, in "Group theory and its application to physical problems", New York: Dover Publications 1989